

Laboratory Study On Mechanical Response And Failure Mechanism of Red-Bed Soft Rock Under Water-Rock Interaction

Chi Liu

Tsinghua University

Xiaoli Liu (✉ xiaoli.liu@tsinghua.edu.cn)

Tsinghua University <https://orcid.org/0000-0002-6204-4485>

Huan Sun

Hainan University

Mingyang Wang

Tsinghua University

Chunlu Wu

Tsinghua University

Enzhi Wang

Tsinghua University

Sijing Wang

Tsinghua University

Research Article

Keywords: Red-bed, Visual experimental platform, Angiography, Convolutional neural network, Water-damaged cracks, Rain-fall-induced landslide

Posted Date: October 1st, 2021

DOI: <https://doi.org/10.21203/rs.3.rs-936170/v1>

License: © ⓘ This work is licensed under a Creative Commons Attribution 4.0 International License. [Read Full License](#)

Abstract

Red-bed soft rock is a geomaterial that displays special deformation and failure characteristics. The stability of red-bed slopes can be negatively impacted by water and stepped excavation disturbance; however, there is limited research regarding the mechanical behavior and failure characteristics of red-bed soft rock under the action of water-rock hydro-mechanical coupling. In this study, to explore the mechanical response and failure mechanisms of red-bed soft rock under coupled water-rock hydro-mechanical action, a visual experimental platform based on digital radiography and a multi-level loading device was constructed. Radiography was used to visualize the rock fracture process by replacing fissure water with a contrast medium. Multi-level loading was applied to cubic red-bed mudstone samples, and acoustic emission signals, stress, flow rate, and digital radiography images were collected during the failure process. An original image processing method based on Hough transform and a convolutional neural network was used to segment and extract cracks from the imagery, and fissure water flow characteristics, rock mechanical response, and crack evolution were analyzed in detail (Liu et al., 2015; Lv et al., 2013, 2014). Results showed that when the Felicity ratio FR was lower than 1.2, water could induce secondary "water-damaged cracks" in the red-bed samples. Study findings were used to highlight the importance of improved early-warning methods for rainfall-induced landslides at an engineering scale. The original experimental platform proposed and evaluated in this study provides a new and powerful tool to investigate the mechanical behavior of different rock types under the action of water-rock hydro-mechanical coupling at a laboratory scale. These findings will facilitate improved disaster prevention strategies for red-bed geological bodies.

1. Introduction

Argillaceous rocks are of interest to engineers due to their wide distribution, sensitivity to environmental factors (e.g., water and external loads), and complex mechanical properties and failure characteristics (Corkum and Martin, 2007). Common in China, red-bed soft rock is considered to be a special kind of argillaceous rock characterized by weak permeability, strong hydrophilicity, and water softening capacity. Argillaceous interlayers (mudstone), are common in Chinese red-bed regions and have a significant influence on engineering stability. According to the statistics from Chai et al. (2014), approximately 18 % of landslides in the Three Gorges Reservoir area occur in these mudstones. With increased engineering activity (e.g., slope stepped excavation), engineering problems (e.g., landslides) related to red-bed soft rock are increasing. Thus, a systematic investigation of the mechanical behavior and failure mechanisms of red-bed soft rock considering factors such as water and loading stress is urgently required.

Numerous studies have examined the mechanical properties of rock. For example, Geertsema (2002) found that the shear strength of mudstone was far lower than expected, which should be considered when designing a dam on argillaceous rock mass with planar joints. Furthermore, loading tests revealed that mudstone deformation and failure under compression was mainly dependent on axial loading and dilatancy in the lateral direction (Wen et al., 2018; Zheng et al., 2018). He et al. (2010) conducted a true triaxial single-face dynamic unloading test on limestone to investigate its acoustic emission (AE) characteristics and found AE signals with a high amplitude and low frequency before the test sample was broken. A direct shear test was also used to study bedding planes formed by purplish-red mudstone and argillaceous limestone from the Three Gorges Reservoir Area (Wu et al., 2018). Results illustrated that bedding planes between intensively weathered mudstone and slightly weathered limestone were the most dangerous potential sliding planes. Environmental scanning electron microscopy (SEM) and digital image correlation techniques have also been used to study the mechanical behavior of mudstone at a microscopic level (Wang et al., 2015). However, none of the aforementioned studies have considered the effect of water on rock degradation.

Water-rock interaction has a considerable impact on rock mechanical strength and failure behavior (Liu et al., 2008a, 2008b; Deng et al., 2016), and studies generally agree that water reduces rock strength (Lin et al., 2013; Liu et al., 2018; Liu et al., 2020; Lu et al., 2017; Wasantha and Ranjith 2014). Water-induced weakening was more apparent in rocks rich in clay compared to those rich in quartz (Grant, 1982; Poulsen et al., 2014). Furthermore, rocks with different clay content would have varying degrees of dilatancy and softening following water absorption, resulting in mechanical strength decline (Erguler and Ulusay,

2009). The strength of mudstone is related to its saturation (water content); that is, the uniaxial compressive strength of rock is either negatively linear or negatively exponentially correlated with water content (Ramos da Silva et al., 2008; Yilmaz, 2010). Jiang et al. (2014) conducted water-mudstone interaction tests and found that weakened mechanical strength was attributed to the physical expansion force generated by the dilatancy of clay minerals following water absorption. Gautam and Shakoor (2013) found that the clay content was a key factor affecting mudstone disintegration and failure. Furthermore, mudstone strength and slope stability was significantly reduced by the drying-wetting cycle (Xu et al., 2018). In recent years, advanced techniques such as SEM and computed tomography (CT) have been used to study microscopic water-induced weakening mechanisms in mudstone, providing a strong basis for researchers to directly observe the mechanical properties of water-weakened rocks (Jiang et al., 2014; Wang et al., 2015; Xiao et al., 2016; Zhang et al., 2012). However, these techniques are not capable of studying the evolution of rock cracks.

Rock failure is a consequence of the initiation, propagation, and connection of cracks. Furthermore, research shows that the combined action of external load and water is the main reason for the mechanical deterioration of red-bed mudstone. However, the evolution of rock cracks is difficult to monitor and observe. Furthermore, evaluating the impact of water flow in cracks on rock mechanical properties remains challenging. The circulatory system of the human body is analogous to the rock internal fracture network. Advanced digital radiography (DR) techniques have provided technical support for understanding changes in human body structure, and enhanced angiography has become an effective means to directly observe and calibrate targets (Hirono et al., 2003). The DR image, which is similar to a CT image, is composed of pixels with different gray levels from black to white, which reflect the X-ray absorption coefficient of the associated voxel (Sheikhzadeh et al., 2019). However, it can be difficult to obtain accurate results from image segmentation methods based on threshold or machine learning techniques due to complex geometric topology, small grayscale differences, and the need to manually design a task-related recognition process (Shi et al., 2016). Consequently, the accurate detection of crack distribution remains challenging at the pixel scale. In recent years, use of the convolutional neural network (CNN) at the pixel scale has been prominent in various deep neural networks because it is capable of self-learning from image samples, showing considerable advantages in terms of image recognition, segmentation, and classification (Ai et al., 2020; Polsinelli et al., 2020; Xu et al., 2019).

Stepped excavation disturbance and water-induced weakening would inevitably lead to deformation and failure, accelerating the instability of the red-bed slope. In this study, a visual experimental platform based on DR and a multi-level loading device was designed and constructed to realize the synchronous visualization of rock fracture processes and fissure water flow. Multilevel loading was applied to red-bed cubic mudstone samples for the collection of AE signals, stress, flow rate, and DR images during the failure process. An original image processing method based on Hough transform (HT) and a CNN was proposed to segment and extract cracks from DR imagery to reveal water-induced damage characteristics and the failure mechanisms of red-bed mudstone under the action of water-rock hydro-mechanical coupling. Finally, we discuss our research findings in the context of early warning index selection for rainfall-type landslides at an engineering scale. The original experimental platform proposed and evaluated in this study provides a new and powerful tool to investigate the mechanical behavior of different rock types under the action of water-rock hydro-mechanical coupling at a laboratory scale. The research findings will help to improve disaster prevention for red-bed geological bodies at an engineering scale.

2. Methodology

2.1. Visual experimental platform

Advanced digital radiography (DR) is an imaging technique used in diagnostic radiology in the medical field. In this technique, a substance, which has a higher or lower density and atomic number, is used in human organs to produce a notable contrast to facilitate differentiation and visualization. In this study, DSM-80 X-ray DR equipment was used to visualize the evolution of rock cracks (Kasap and Rowlands, 2002; Sun, 2017). To investigate the failure mechanisms of red-bed mudstone under the action of water-rock hydro-mechanical coupling, a multi-level loading device matching the DR system was developed (Fig. 1) (Sun et al., 2021). The visual experimental platform for rock crack evolution was built based on the DR system and multilevel loading device, as shown in Fig. 2.

The multilevel loading device was composed of an upper, middle, and bottom panel. The upper and bottom panels were fixed by a steel cylindrical rod while the middle panel could slide up and down the rod. Nylon material was used as an inner tube to reduce sliding friction. A manually controlled hydraulic jack was used to drive the middle panel upwards to realize uniaxial compression loading on the rock specimen. A spoke stress sensor with an accuracy of $\pm 1\%$ was installed under the upper panel and a video graphics array interface was used to connect a computer to monitor and record the stress. A SAEU3S centralized AE monitoring system was used to obtain AE data during the rock fracture process. The basic thresholds for AE monitoring is summarized in Table 1. The AE probes were fixed on the surface of the cubic red-bed rock specimen and connected to an amplifier, data acquisition host, and the computer terminal. A self-priming pump and two flowmeters were used to inject contrast medium with a water pressure of approximately 0.8 MPa and record the flow rate, respectively. The parameters of the self-priming pump and flowmeters are shown in Tables 2 and 3. The rock samples used in this paper were taken from the location K2 + 200 at the Chuanda Highway, Qinghai Province and were processed to a cubic specimen size of $10 \times 10 \times 10$ cm with a 3 mm diameter tube in the center of the specimen. The main mineral composition of these rock samples was quartz, albite, clinocllore, muscovite and hematite (Fig. 3), with relative contents of 40.9%, 33.1%, 9.32%, 1.38% and 15.3%, respectively.

Table 1
Threshold parameters used in AE testing

Parameters	Channel threshold (mV)	Hit definition time (μ s)	Maximum definition time (μ s)	Sampling frequency (MHz)	Filter control		
					Maximum limiting	Minimum limiting	Filter threshold (mV)
					frequency (kHz)	frequency (kHz)	
Value	100	2000	500	6	400	100	20

Table 2
Self-priming pump parameters

Model	Rated current/A	Inlet flow rate/ $L \cdot \text{min}^{-1}$	Motor speed/ $r \cdot \text{min}^{-1}$	Maximum head/m
LS-0412	1.2	2.0	2200	30

Table 3
Flowmeter parameters

Model	Normal range of flow rate/ $\text{m}^3 \cdot \text{h}^{-1}$	Bearing stress/MPa
DN4	0.04 ~ 0.25	6.30

2.2. Image processing method

Crack evolution in the DR images was visualized by replacing water with a contrast medium according to the difference in the X-ray absorption coefficient for different components, i.e., angiography. Notably, the contrast medium in the cracks extended to the tube; thus, the imaging effect of cracks enhanced by the contrast medium showed bands of white spots with different brightness at the pixel scale.

In this paper, an original image processing method based on median filter, HT, and CNN was proposed to segment and extract cracks in DR images, as shown in Fig. 4. The median filter algorithm can reduce image noise while maintaining its original boundary. This is a typical pre-processing step which can improve the results in subsequent processing such as edge detection or segmentation (Huang, 1979). Furthermore, HT is a basic method to recognize geometry such as circles and lines (Hough, 1962; Wang et al., 2019). The basic principle of HT is to use point and line duality to convert a line in the original image to a point; that is, to transform the detection of overall characteristics into the detection of local characteristics to reduce the computational burden of subsequent identification. The CNN uses filters composed of several layers with different functions

to encode the existing images and vectorize part of the input image information into the new matrix through convolution computation (Schmidhuber and Jürgen 2015). The useful information in the new matrix can be extracted by pooling layers to reduce the size of the matrix. Then, the updated weight matrix is propagated backwards using the activation and loss functions to achieve the segmentation and extraction of local features (e.g., cracks) in the target object (e.g., rocks). The noise-reduced DR images were vectorized using MATLAB R2019a, irrelevant background data was removed to segment the region of interest using HT, and the pre-trained CNN was used to automatically extract useful geometry (Fig. 5).

3. Results

3.1. Flow characteristics

Figure 5 shows that the inlet and outlet flow rate of the test specimen fluctuate markedly and the flow rate curve displays an apparent zigzag shape, attributed to water absorption characteristics (Fig. 7b) and red-bed soft rock softening. Water flow softened the tube wall of the samples and exfoliated some particles from the wall surface, increasing the tube wall roughness and unstable flow state. As water scoured the tube wall, exfoliated argillaceous particles were entrained in the water due to hydrodynamic action, increasing its turbidity (Fig. 8). The inlet flow rate was always greater than that of the outlet, and we attribute this to frictional and local head loss. Consequently, the outlet flow velocity was lower compared to that at the inlet based on the energy conservation law. Because the tube diameter was the same, the flow rate evolution was the same as that of flow velocity. However, the DN4 flowmeters used in this study have a high sensitivity, and small exfoliated argillaceous particles would block the rotation of induction blade inside the flowmeter resulting in unusual instantaneous data readings and a sudden drop in flow rate (Fig. 6d).

3.2. Stress and AE coupling characteristics

The Kaiser effect reflects the memory of AE characteristics under historical loads during fracture process, i.e. no obvious AE signal occurs before the repeated loading reaches the maximum stress previously applied. However, the anti-Kaiser effect, also known as the Felicity effect, is a phenomenon that the notable AE signal appears when the repeated loading is lower than the historical maximum stress, which usually indicates that critical damage has occurred in materials like rocks. The Felicity ratio FR is a quantitative parameter that can reflect the damage degree of a material. The FR can be calculated as follows:

$$FR = \frac{\sigma_{AE}}{\sigma_{max}}$$

1

where σ_{AE} and σ_{max} are the stress corresponding to the initial AE signal during the repeated loading and the previous maximum stress, respectively. If $FR > 1$, the Kaiser effect is present; if $FR < 1$, the Felicity effect is present.

Previous studies have shown that AE signals during the steady stage of uniaxial multilevel loading were very small; however, they increased significantly during the loading stage (Zhang et al., 2006). Figure 9 illustrates the relationship between stress and the AE signal for four red-bed mudstone samples, named RBSR01, RBSR02, RBSR03, and RBSR04, respectively, under uniaxial multilevel loading and hydrodynamic action. At the beginning of the experiment, the sudden increase in the AE signal (ringing count and energy count) occurred at or shortly before and after the single-level stress loading stage, indicating that external loads played a leading role in red-bed mudstone sample damage when the stress was small. The AE signal gradually increased during the steady loading stage, indicating that accumulated deformation and damage would make water-induced damage more apparent when the stress was large. Water flowed into the cracks and continued to develop pre-existing cracks, producing large secondary water-damaged cracks. According to the calculated FR (seen in Table 4) and Fig. 9, when FR was greater than 1.2, the significant increase of AE signal almost occurred in the loading stage; when FR was lower than 1.2, the similar AE signal can be gradually seen in the steady stage. Thus, the FR could be a possible parameter and the value of FR equal to approximately 1.2 was the threshold to evaluate whether the secondary water-damaged cracks existed. The specific failure mechanism of water-damaged cracks is discussed further in Sect. 4. When the Kaiser effect of AE signal changed to Felicity effect, i.e. FR changed from greater than 1 to less than 1, the corresponding stress was the peak stress. In addition,

according to Figs. 9 (a–h), the peak loading of RBSR01, RBSR02, RBSR03, and RBSR04 corresponded with loading levels 7 (5 MPa), 15 (18.5 MPa), 5 (5.93 MPa), and 4 (4.51 MPa), respectively. This indicates that RBSR02 was harder than RBSR01, RBSR03, and RBSR04. The abrupt drop in the stress curve at the moment of rock failure in Figs. 9 (a–f) indicates that RBSR01, RBSR02, and RBSR03 had certain brittle failure characteristics, while the gradual decline of the stress curve in Figs. 9 (g) and (h) reveals no apparent brittleness in RBSR04.

Table 4
Ratios of two consecutive loads during the fracture process of each red-bed mudstone specimen

Sample number	Ratios of two consecutive loads													
	σ_2/σ_1	σ_3/σ_2	σ_4/σ_3	σ_5/σ_4	σ_6/σ_5	σ_7/σ_6	σ_8/σ_7	σ_9/σ_8	σ_{10}/σ_9	σ_{11}/σ_{10}	σ_{12}/σ_{11}	σ_{13}/σ_{12}	σ_{14}/σ_{13}	σ_{15}/σ_{14}
RBSR01	5.16	1.32	1.28	1.22	1.18	1.15	1.09*	0.91	0.48	0.87	1.00	0.58	N/A	N/A
RBSR02	1.50	1.39	1.31	1.26	1.21	1.17	1.14	1.07	1.09	1.09	1.08	1.09	1.08	1.11*
RBSR03	1.37	1.54	1.39	1.19*	0.88	0.29	N/A	N/A	N/A	N/A	N/A	N/A	N/A	N/A
RBSR04	1.53	1.43	1.10*	0.68	0.36	0.41	N/A	N/A	N/A	N/A	N/A	N/A	N/A	N/A

The * symbol represents the critical *FR* before rock failure

3.3. Failure characteristics and crack evolution

Under axial multilevel loading, the samples demonstrated a failure mode dominated by tensile failure (Fig. 10). Due to the Poisson effect of geomaterials, obvious lateral dilatancy was observed when the lateral tensile stress exceeded the tensile strength of the rock, generating cracks that were nearly parallel to the direction of loading. However, some cracks deviated considerably from the loading axis near the lateral boundaries of the rock samples (Fig. 11).

To investigate the evolution of red-bed soft rock under the action of water-rock hydro-mechanical coupling, the image processing method described in Sect. 2.2 was used to segment and extract cracks from DR images of RBSR04 as shown in Fig. 12. This sample was chosen because all four rock samples displayed similar macroscopic failure modes. According to the diagram of crack distribution in Figs. 12 (a2–e2), the corresponding fractal dimension, average crack width, damaged area (Fig. 13), and crack orientation rose diagram (Fig. 14) were calculated and plotted.

The cracks in RBSR04 shown in Figs. 12 (a1) and (a2) do not correspond to the first loading and initial cracking, rather they correspond to the second loading stage in Figs. 9 (g) and (h). The fractal dimension, average crack width, and percentage of damage area all fluctuated to a certain extent. When the rock sample reached the stress peak corresponding to the fourth loading stage in Figs. 9 (g) and (h) and 12 (c1) and (c2), and the third loading time in Fig. 13, the damaged area increased to 3.64 %, indicating that damage was still occurring. However, the fractal dimension (1.69 mm) and average crack width (0.994 mm) decreased significantly. One possible reason is that parameter values were related to crack resolution, which was positively correlated with the volume of contrast medium in the crack. When the rock was damaged, cracks penetrated the rock surface, resulting in the loss of contrast medium and a failure to segment and extract certain cracks. Furthermore, original cracks may have closed during loading. Although new cracks would be formed constantly, the contrast medium inlet was relatively small and the fluid may not have reached these new cracks.

According to the fitting curves in Fig. 13, the fractal dimension, average crack width, and damaged area increased quickly during the initial stages of crack propagation, attributed to many large cracks developing in a relatively short period. In other words, the red-bed mudstone accumulated numerous cracks during the early loading stages. When the number of accumulated cracks reached a certain level, large cracks could be seen in the DR images. At peak loading, the fractal

dimension, average crack width, and damaged area still increased; however, the growth rate decreased gradually, indicating that crack evolution slowed down following rock failure.

Figure 14 shows a rose diagram of the possible distribution of crack orientation, the radius of which represents the proportion of cracks distributed in a certain interval. The crack strike was mainly concentrated within $\pm 30^\circ$ of the loading axis. As the loading time increased, the crack strike gradually deviated away from the loading axis.

4. Discussion

It is well known that water sensitivity and external disturbance are key problems in red-bed soft rock areas. The water sensitivity of red-bed soft rock depends on its clay mineral content; more clay minerals increase the sensitivity of red-bed soft rock to water. The aforementioned mineral composition of red-bed mudstone in this study was mainly quartz, albite, clinocllore, muscovite and hematite, whereas its clay mineral content (e.g., kaolinite, illite, and montmorillonite) was too low to detect by XRD. Therefore, the water softening and disintegration effects observed in this study were not large. In Sect. 3.2, we proposed the concept of water-damaged cracks. In our experiment, the water pressure provided by the self-priming pump was relatively low (approximately 0.8 MPa). However, this low water pressure could still cause crack propagation and connection because red-bed rock is relatively soft compared to rocks such as granite and sandstone. Consequently, we consider water-damaged cracks to be hydraulic fracturing type cracks. Future research will focus on adopting SEM or CT techniques to conduct microscopic and mesoscopic analysis on the failure surface to determine the specific failure mechanism of water-damaged cracks. Uniaxial multilevel loading at the laboratory scale was adopted in this study to correspond with stepped excavation disturbance at an engineering scale. However, engineers may pay more attention to unloading effects, which corresponds with multilevel unloading or the multilevel loading and unloading cycle at the laboratory scale. Therefore, future studies will focus on improving the visual experimental platform under the action of water-force coupling. Cracks visualized in DR images are actually the projection of three-dimensional (3D) cracks on a two-dimensional (2D) plane. However, due to the good integrity and invisible bedding surfaces of red-bed mudstone, the rock samples are regarded as isotropic bodies in this study. Considering the randomness of spatial crack evolution, 2D crack evolution, at least statistically, can reflect 3D crack evolution.

The research findings in this study are important for the understanding of risks associated with red-bed geological bodies at an engineering scale. Our findings show that water does not contribute markedly to the damage of red-bed samples under low loading stress. Conversely, the impact of water on crack formation is considerable under high loads. This is because when the loading stress is low, deformation and damage to the intact rock is minimal and the openings of internal microcracks are small. Furthermore, poor crack connectivity and permeability make it difficult for water to enter the cracks. When the external loads are large, cumulative deformation and damage facilitate the connection of internal cracks, leading to the formation of many large cracks. Pressurized water flow within the cracks promotes further crack propagation. Based on these findings, we conclude that the action of water may not induce obvious damage to red-bed rocks without the action of a load, regardless of the rock deformation. In the western mountainous areas of China, where heavy rainfall is prevalent, large-scale red-bed landslides have been caused by human activities (e.g., excavation disturbance during highway and railway construction). Considering the water sensitivity of red-bed slopes, early warning systems for rainfall-type landslides are particularly important. The most commonly used early warning method is currently the rainfall threshold warning. However, according to the stress-AE coupling relationship described in Sect. 3.2 and the aforementioned analysis, there are obvious hidden dangers in using rainfall as the only early warning index to evaluate landslide risk, even though the red-bed geological body is usually affected by water at the engineering scale. Although the rainfall threshold early warning method has achieved remarkable results in the early warning and disaster prevention of rainfall-induced landslides in China, the increasing number of false and missing warnings has eroded confidence in the index.

A combined index that considers variations in groundwater levels and slope deformation has been suggested as an alternate warning system for rainfall-induced landslides. The variation of groundwater levels in a landslide, which is positively correlated with the rainfall infiltration coefficient (or permeability) of rock and soil mass, is an important factor impacting slope

stability. However, the rainfall infiltration coefficient varies considerably between regions due to different material composition and topography. Even in heavy rainfall, rainwater cannot reach the potential sliding geological body due to the low permeability of the rock and soil mass, so the water-induced weakening effect on the red-bed slope is significantly reduced. Furthermore, slope instability is based on accumulated deformation, which increases the permeability of the rock and soil mass, resulting in the water infiltration in the potential sliding mass, enhancing water-induced deterioration, and increasing the likelihood of a red-bed landslide. Therefore, monitoring groundwater levels and slope deformation directly is more reliable compared to monitoring rainfall alone. Groundwater levels and slope deformation were used as early warning indices by Xu et al., (2020) and were found to greatly improve the accuracy of early warning systems for red-bed landslides.

Although the visual experimental platform under the action of water-rock hydro-mechanical coupling evaluated in this study has some limitations, our research findings regarding the failure mechanisms of red-bed soft rock provide laboratory scale support for the selection of early warning systems for rainfall-induced landslides at an engineering scale.

5. Conclusion

The stability of red-bed slopes is greatly impacted by water infiltration and stepped excavation disturbance. To investigate the characteristics of red-bed soft rock under the action of water-rock hydro-mechanical coupling, a visual experimental platform using DR and a multi-level loading device was constructed. Angiography was used to visualize crack evolution by replacing fissure water with a medical contrast medium. An original image processing method based on HT and CNN was then proposed to segment and extract cracks during the red-bed mudstone failure process. According to AE signals, stress, flow rate, and crack distribution in DR images during the failure process, we analyzed the flow characteristics of fissure water, the mechanical response of red-bed mudstone, and crack evolution. Research findings are as follows:

- (1) Red-bed mudstone is characterized by obvious water absorption and a brittle failure mode.
- (2) The Felicity ratio FR can be a parameter to evaluate whether the secondary "water-damaged cracks" exist. When FR was lower than 1.2, water can induce secondary "water-damaged cracks".
- (3) Red-bed mudstone samples demonstrated a failure mode dominated by tensile failure under the action of axial multilevel loading. As the loading time increased, crack strikes deviated from an orientation that was approximately parallel to the loading axis.
- (4) According to the destructive mechanisms of water and deformation on red-bed geological bodies, an index which combines groundwater level and slope deformation monitoring is recommended as an early warning index for rainfall-type landslides.

Although the original visual experimental platform developed in this study has some limitations with respect to the loading mode and 3D crack imaging, it provides a new and powerful tool to investigate the mechanical behavior of different rock types under the action of water-rock hydro-mechanical coupling at a laboratory scale. Our research findings will help to improve early warning systems and disaster prevention for red-bed geological bodies at an engineering scale.

Abbreviations

AE, acoustic emission; CNN, convolutional neural network; HT, Hough transform.

Declarations

Funding This work was supported by the National Key R&D Program of China (Grant No. 2018YFC1504902), and the National Natural Science Foundation of China (Grant No. 52079068, 41772246, 41941019), and the State Key Laboratory of Hydrosience and Hydraulic Engineering (Grant No. 2021-KY-04).

Conflict of interest The authors confirm that they have no conflict of interest.

References

1. Ai D, Jiang G, Lam S-K, He P, Li C (2020) Automatic pixel-wise detection of evolving cracks on rock surface in video data. *Autom Constr* 119:103378. doi:<https://doi.org/10.1016/j.autcon.2020.103378>
2. Chai B, Tong J, Jiang B, Yin K (2014) How does the water–rock interaction of marly rocks affect its mechanical properties in the Three Gorges reservoir area. China? *Environmental Earth Sciences* 72:2797–2810. doi:10.1007/s12665-014-3204-y
3. Corkum AG, Martin CD (2007) The mechanical behaviour of weak mudstone (Opalinus Clay) at low stresses. *Int J Rock Mech Min Sci* 44:196–209. doi:<https://doi.org/10.1016/j.ijrmms.2006.06.004>
4. Deng HF, Zhou ML, Li JL, Sun XS, Huang YL (2016) Creep degradation mechanism by water-rock interaction in the red-layer soft rock. *Arab J Geosci* 9:601. doi:10.1007/s12517-016-2604-6
5. Erguler ZA, Ulusay R (2009) Water-induced variations in mechanical properties of clay-bearing rocks. *Int J Rock Mech Min Sci* 46:355–370. doi:<https://doi.org/10.1016/j.ijrmms.2008.07.002>
6. Gautam TP, Shakoor A (2013) Slaking behavior of clay-bearing rocks during a one-year exposure to natural climatic conditions. *Eng Geol* 166:17–25. doi:<https://doi.org/10.1016/j.enggeo.2013.08.003>
7. Geertsema AJ (2002) The shear strength of planar joints in mudstone. *Int J Rock Mech Min Sci* 39:1045–1049. doi:[https://doi.org/10.1016/S1365-1609\(02\)00100-4](https://doi.org/10.1016/S1365-1609(02)00100-4)
8. Grant K (1982) Introduction to Rock Mechanics. *Eng Geol* 19:72–74. doi:[https://doi.org/10.1016/0013-7952\(82\)90015-1](https://doi.org/10.1016/0013-7952(82)90015-1)
9. He MC, Miao JL, Feng JL (2010) Rock burst process of limestone and its acoustic emission characteristics under true-triaxial unloading conditions. *Int J Rock Mech Min Sci* 47:286–298. doi:<https://doi.org/10.1016/j.ijrmms.2009.09.003>
10. Hirono T, Takahashi M, Nakashima S (2003) In situ visualization of fluid flow image within deformed rock by X-ray CT. *Eng Geol* 70:37–46. doi:[https://doi.org/10.1016/S0013-7952\(03\)00074-7](https://doi.org/10.1016/S0013-7952(03)00074-7)
11. Hough BP (1962) Methods and means for recognizing complex pattern
12. Huang TS (1979) A fast two-dimensional median filtering algorithm. *IEEE Transon Acousticspeech Signal Processing* 27:13–18
13. Jiang Q, Cui J, Feng X, Jiang Y (2014) Application of computerized tomographic scanning to the study of water-induced weakening of mudstone. *Bull Eng Geol Env* 73:1293–1301. doi:10.1007/s10064-014-0597-5
14. Kasap SO, Rowlands JA (2002) Direct-conversion flat-panel X-ray image sensors for digital radiography. *Proceedings of the IEEE*, **90**, 591–604
15. Lin P, Liu X, Hu Y, Xu W, Li Q (2013) Deformation stability analysis of Xiluodu arch dam under stress-seepage coupling condition. *Chin J Rock Mechan Eng* 32(6):1145–1156 (In Chinese)
16. Liu B, Yang H, Karekal S (2020) Effect of Water Content on Argillization of Mudstone During the Tunnelling process. *Rock Mech Rock Eng* 53:799–813. doi:10.1007/s00603-019-01947-w
17. Liu X, Wang S, Wang E, Wang J, Hu B (2008a) Evolutionary rules of flaws in rock subjected to uniaxial compression and rock strength. *Chin J Rock Mechan Eng* 27:1195–1201 (In Chinese)
18. Liu X, Wang E, Wang S, Fan Y (2008b) Representation method of fractured rock mass and its hydraulic properties study. *Chin J Rock Mechan Eng* 27:1814–1821 (In Chinese)
19. Liu X, Wang S, Wang S, Wang E (2015) Fluid-driven fractures in granular materials. *Bull Eng Geol Env* 74:621–636
20. Liu X, Han G, Wang E, Wang S, Nawnit K (2018) Multiscale hierarchical analysis of rock mass and prediction of its mechanical and hydraulic properties. *J Rock Mech Geotech Eng* 10:694–702
21. Lv QF, Liu XL, Wang EZ, Wang SJ (2013) Analytical solution to predicting gaseous mass flow rates of microchannels in a wide range of Knudsen numbers. *Phys Rev E* 88:013007
22. Lv QF, Wang EZ, Liu XL, Wang SJ (2014) Determining the intrinsic permeability of tight porous media based on bivelocity hydrodynamics. *Microfluid Nanofluid* 16:841–848

23. Lu Y, Wang L, Sun X, Wang J (2017) Experimental study of the influence of water and temperature on the mechanical behavior of mudstone and sandstone. *Bull Eng Geol Env* 76:645–660. doi:10.1007/s10064-016-0851-0
24. Polsinelli M, Cinque L, Placidi G (2020) A light CNN for detecting COVID-19 from CT scans of the chest. *Pattern Recogn Lett* 140:95–100. doi:https://doi.org/10.1016/j.patrec.2020.10.001
25. Poulsen BA, Shen B, Williams DJ, Huddleston-Holmes C, Erarslan N, Qin J (2014) Strength reduction on saturation of coal and coal measures rocks with implications for coal pillar strength. *Int J Rock Mech Min Sci* 71:41–52. doi:https://doi.org/10.1016/j.ijrmms.2014.06.012
26. Ramos da Silva M, Schroeder C, Verbrugge J-C (2008) Unsaturated rock mechanics applied to a low-porosity shale. *Eng Geol* 97:42–52. doi:https://doi.org/10.1016/j.enggeo.2007.12.003
27. Schmidhuber & Jürgen (2015) Deep Learning in Neural Networks: An Overview. *Neural Netw* 61:85–117
28. Sheikzadeh M, Vercnocke AJ, Tao S, Rajendran K, Leng S, Ritman EL, McCollough CH (2019) Impact of Effective Detector Pixel and CT Voxel Size on Accurate Estimation of Blood Volume in Opacified Microvasculature. *Academic Radiology* 26:1410–1416. doi:https://doi.org/10.1016/j.acra.2018.11.013
29. Shi Y, Cui L, Qi Z, Meng F, Chen Z (2016) Automatic Road Crack Detection Using Random Structured Forests. *IEEE Trans Intell Transp Syst* 17:3434–3445. doi:10.1109/TITS.2016.2552248
30. Sun H (2017) Research on coupling mechanism and application of stress-fracture-seepage in excavation coal-rock. Xi'an University of Science and Technology, (in Chinese)
31. Sun H, Liu X, Ye Z, Wang E (2021) Experimental investigation of the nonlinear evolution from pipe flow to fissure flow during carbonate rock failures. *Bulletin of Engineering Geology and the Environment*
32. Wang J, Fu P, Gao RX (2019) Machine vision intelligence for product defect inspection based on deep learning and Hough transform. *J Manuf Syst* 51:52–60
33. Wang LL, Bornert M, Héripré E, Chanchole S, Pouya A, Halphen B (2015) The Mechanisms of Deformation and Damage of Mudstones: A Micro-scale Study Combining ESEM and DIC. *Rock Mech Rock Eng* 48:1913–1926. doi:10.1007/s00603-014-0670-1
34. Wasantha PLP, Ranjith PG (2014) Water-weakening behavior of Hawkesbury sandstone in brittle regime. *Eng Geol* 178:91–101. doi:https://doi.org/10.1016/j.enggeo.2014.05.015
35. Wen T, Tang H, Ma J, Wang Y (2018) Evaluation of methods for determining crack initiation stress under compression. *Eng Geol* 235:81–97. doi:https://doi.org/10.1016/j.enggeo.2018.01.018
36. Wu Q, Xu Y, Tang H, Fang K, Jiang Y, Liu C, Wang L, Wang X, Kang J (2018) Investigation on the shear properties of discontinuities at the interface between different rock types in the Badong formation. *China Engineering Geology* 245:280–291. doi:https://doi.org/10.1016/j.enggeo.2018.09.002
37. Xiao Y, Lu J-H, Wang C-P, Deng J (2016) Experimental Study of High-Temperature Fracture Propagation in Anthracite and Destruction of Mudstone from Coalfield Using High-Resolution Microfocus X-ray Computed Tomography. *Rock Mech Rock Eng* 49:3723–3734. doi:10.1007/s00603-016-1006-0
38. Xu C, Sun Q, Yang X (2018) A study of the factors influencing the occurrence of landslides in the Wushan area. *Environ Earth Sci* 77:406. doi:10.1007/s12665-018-7584-2
39. Xu Q (2020) Understanding the landslide monitoring and early warning: consideration to practical issues. *Journal of Engineering Geology* 028(002):360–374. (in Chinese)
40. Xu X, Zhou F, Liu B, Fu D, Bai X (2019) Efficient Multiple Organ Localization in CT Image using 3D Region Proposal Network. *IEEE Transactions on Medical Imaging*, 1–1
41. Yilmaz I (2010) Influence of water content on the strength and deformability of gypsum. *Int J Rock Mech Min Sci* 47:342–347. doi:https://doi.org/10.1016/j.ijrmms.2009.09.002
42. Zhang N, He M, Liu P (2012) Water vapor sorption and its mechanical effect on clay-bearing conglomerate selected from China. *Eng Geol* 141–142:1–8. doi:https://doi.org/10.1016/j.enggeo.2012.04.007

43. Zhang R, Xie HP, Liu JF, Deng JH, Peng Q (2006) Experimental study on acoustic emission characteristics of rock failure under uniaxial multilevel loadings. Chinese Journal of Rock Mechanics and Engineering. 25(12). (in Chinese)
44. Zheng Y, Chen C, Liu T, Zhang W, Song Y (2018) Slope failure mechanisms in dipping interbedded sandstone and mudstone revealed by model testing and distinct-element analysis. Bull Eng Geol Env 77:49–68. doi:10.1007/s10064-017-1007-6

Figures

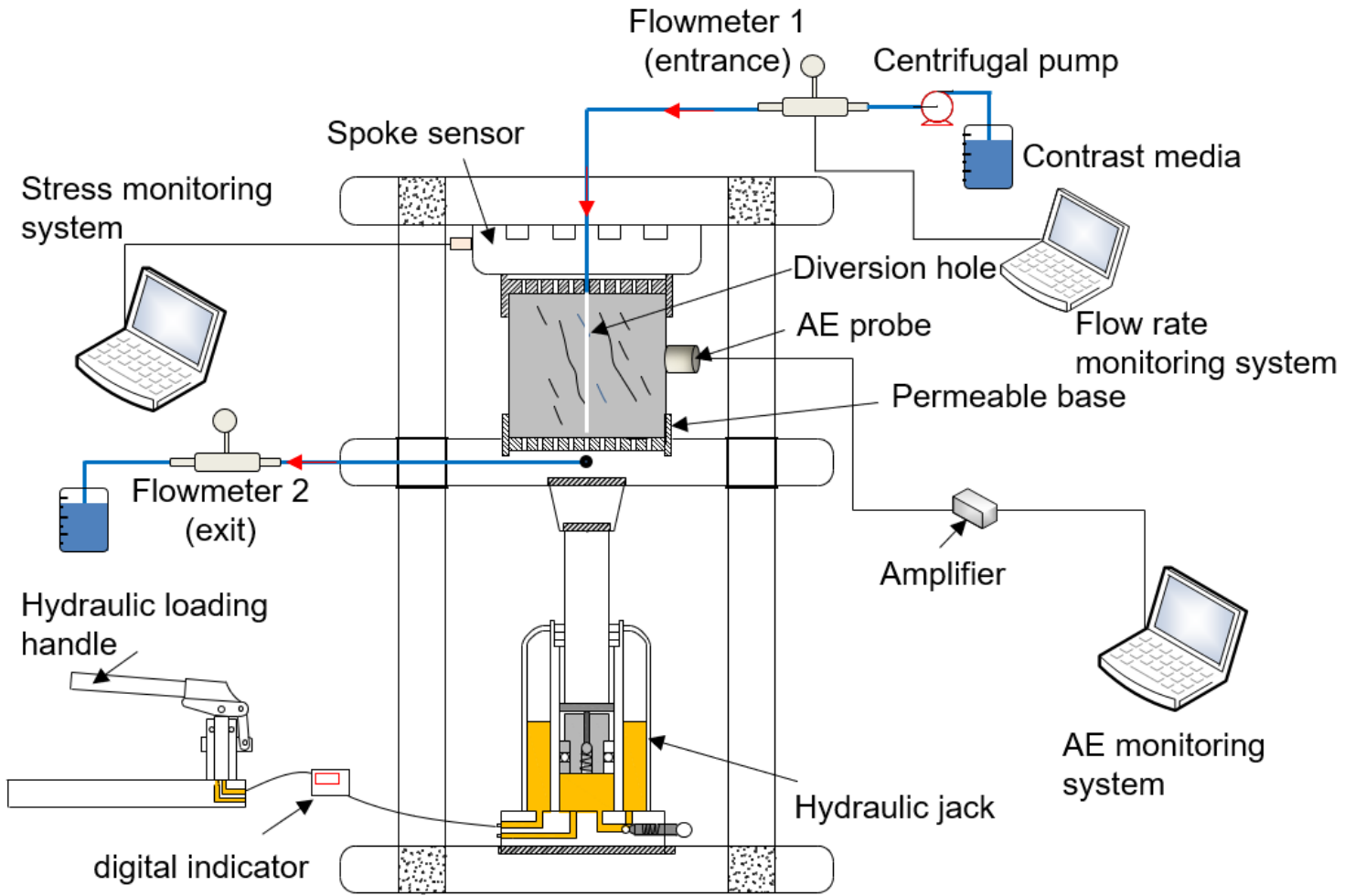


Figure 1

The design of the multilevel loading device for the digital radiography (DR) system

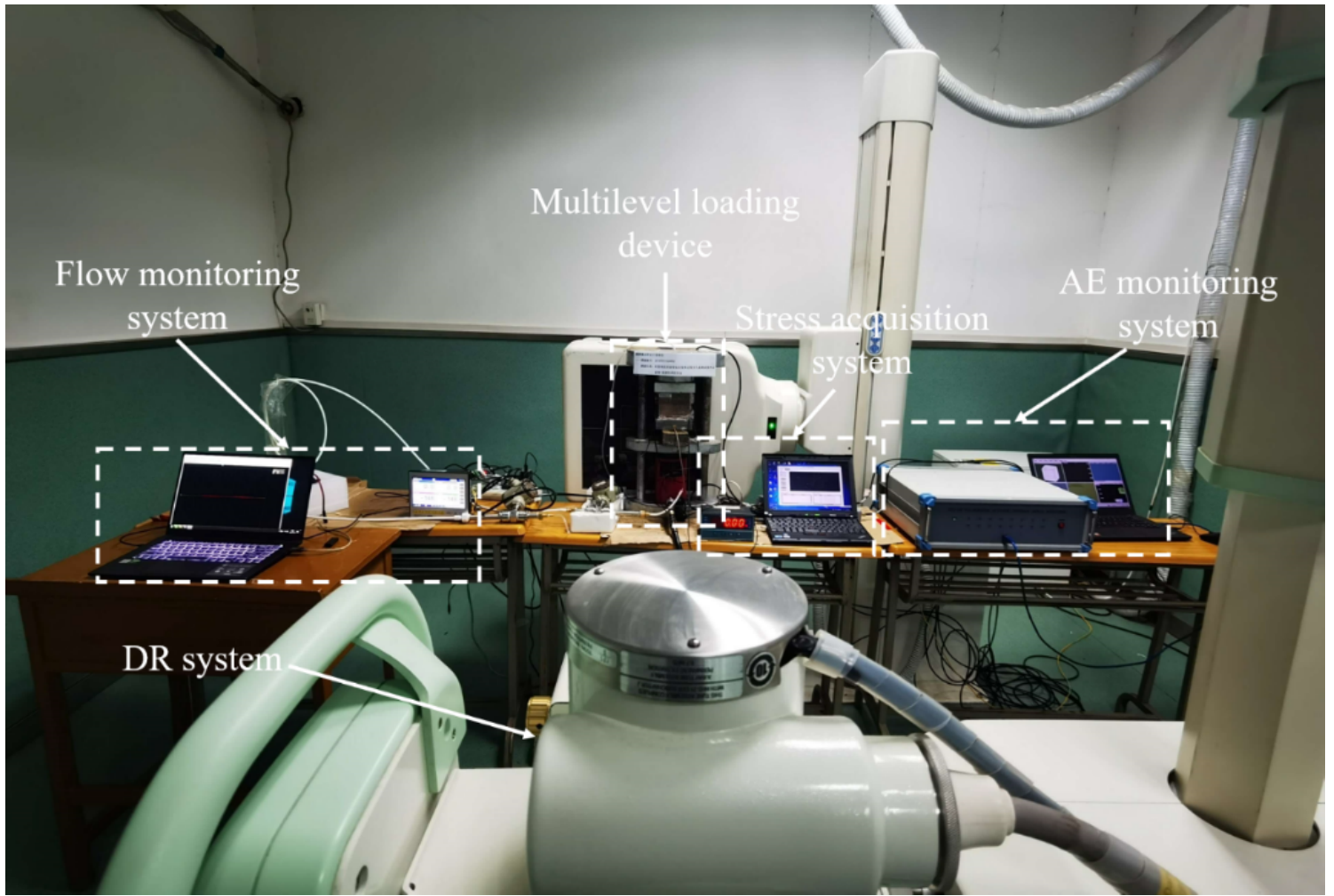


Figure 2

The experimental platform for visualizing rock crack evolution

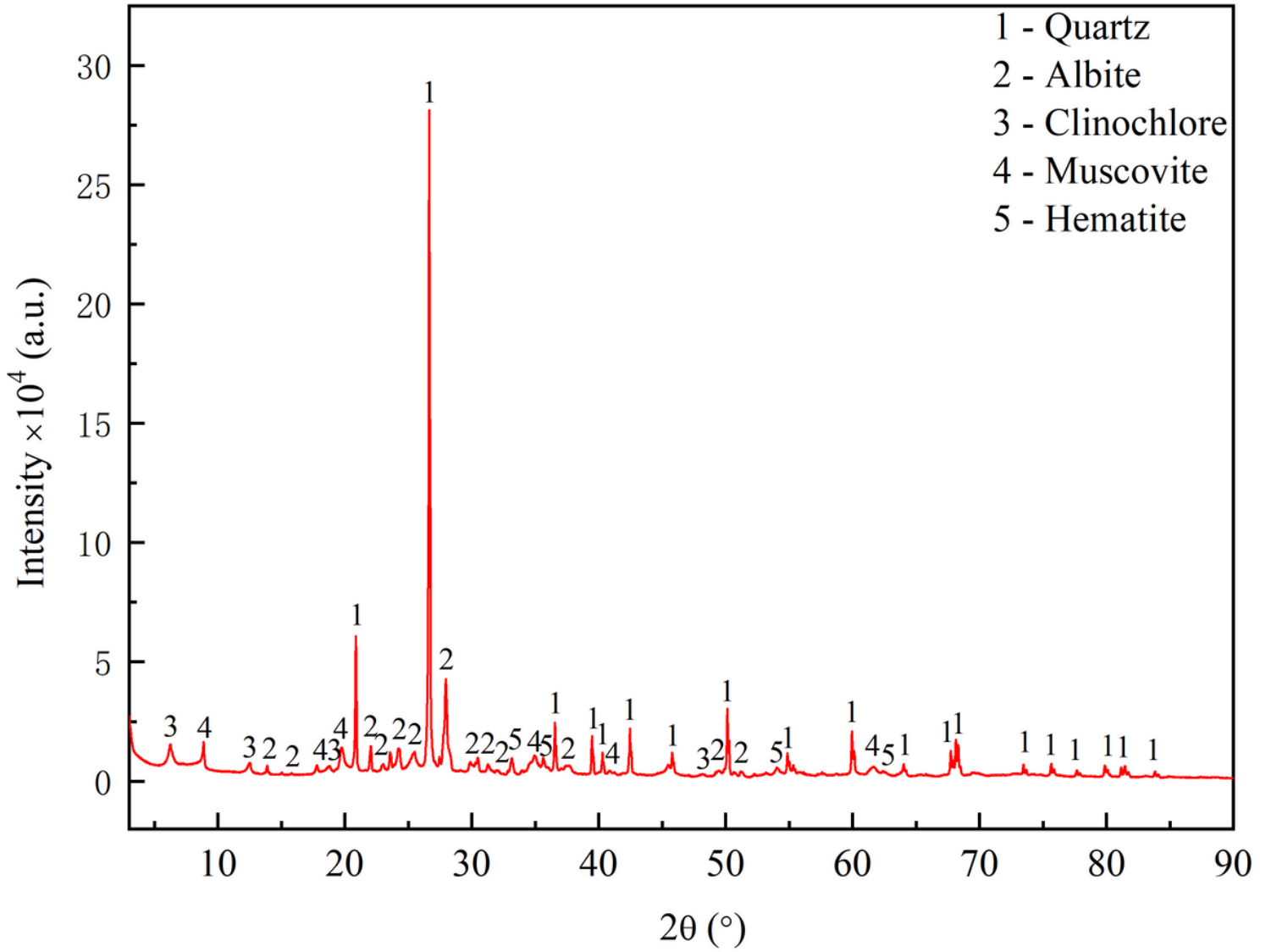


Figure 3

The main mineral composition of red-bed mudstone

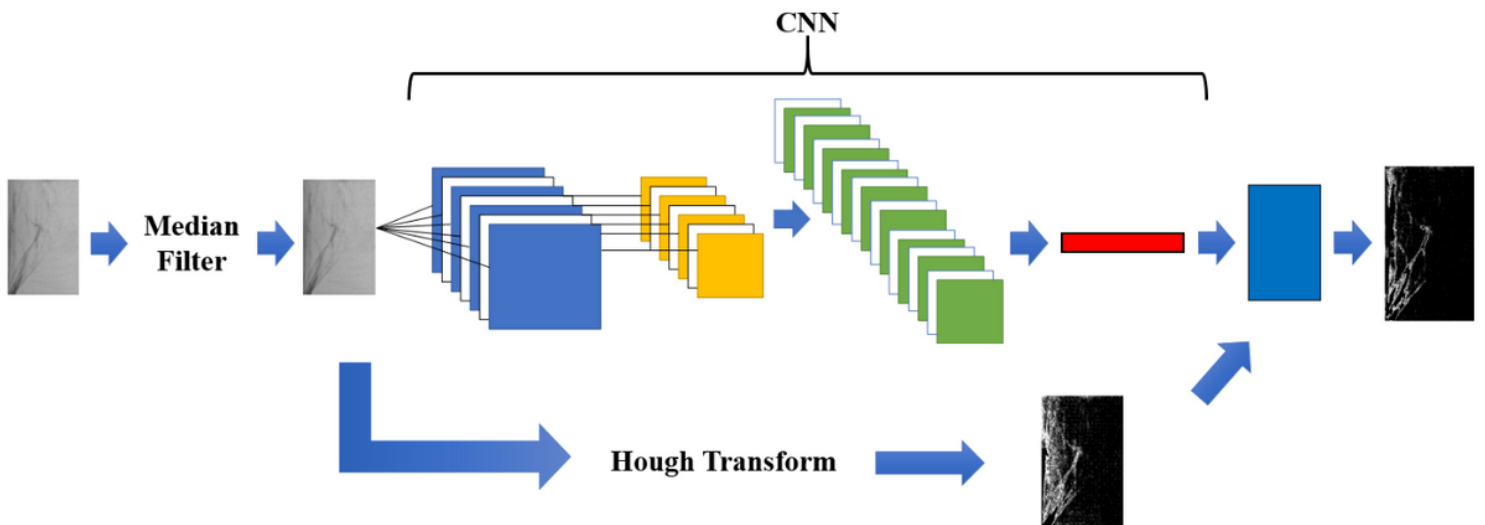


Figure 4

The image processing method

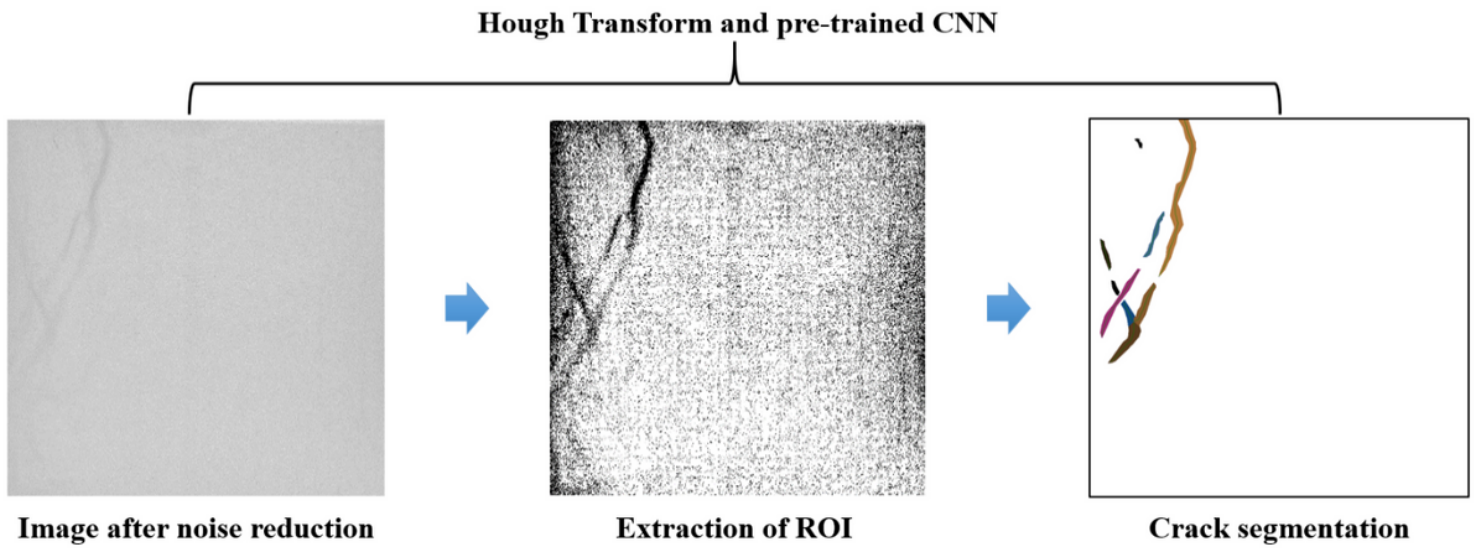


Figure 5

An example of crack segmentation and extraction

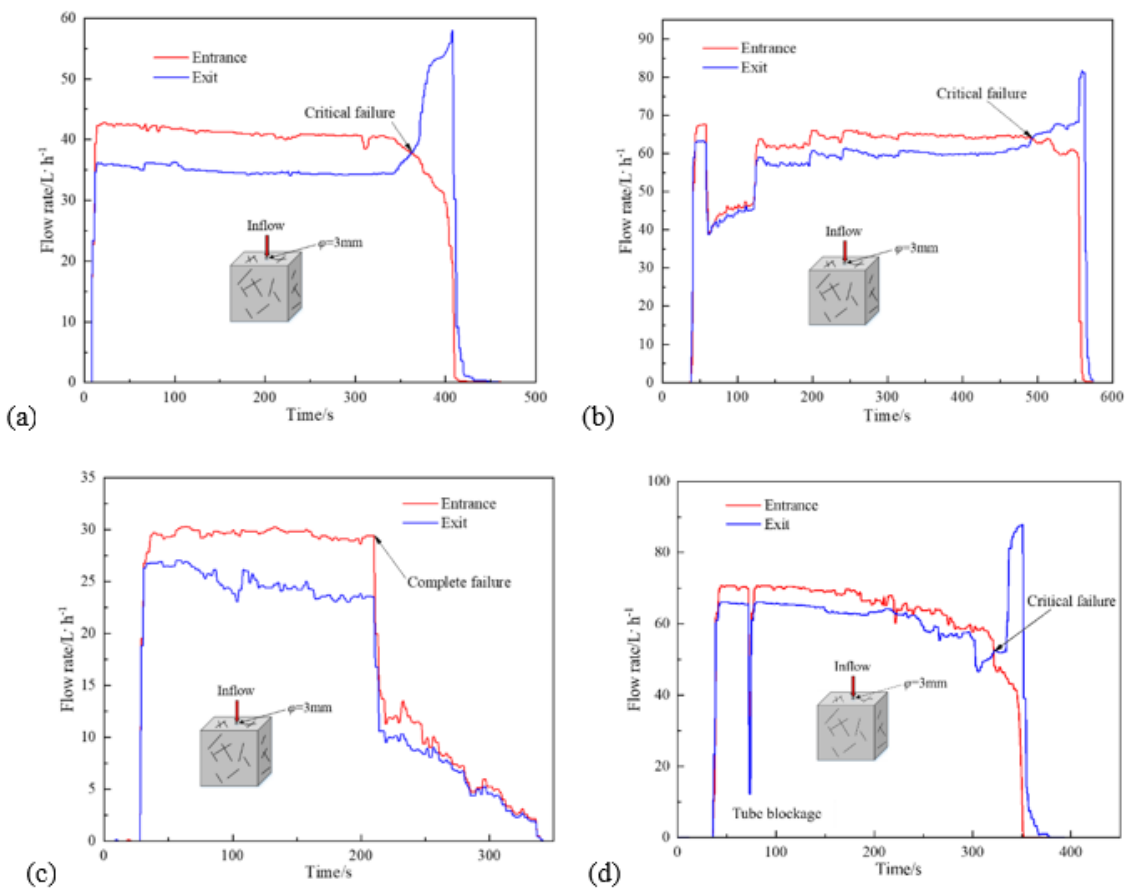


Figure 6

Flow rate curves for the red-bed soft rock (RBSR) samples (a) RBSR01, (b) RBSR02, (c) RBSR03, and (d) RBSR04

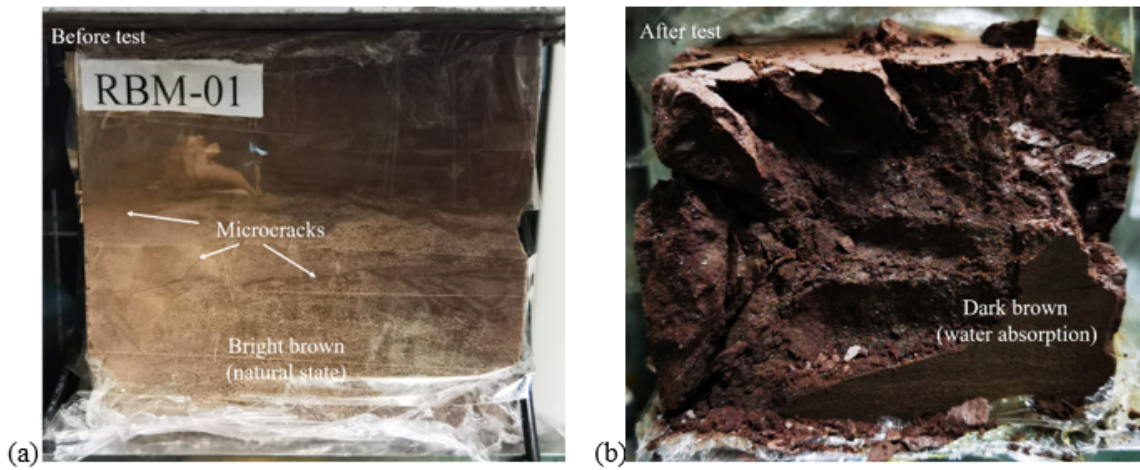


Figure 7

Comparison of surface characteristics for red-bed mudstone before and after water absorption showing (a) microcracks visible on the surface (light brown) and (b) the dark brown surface after absorption

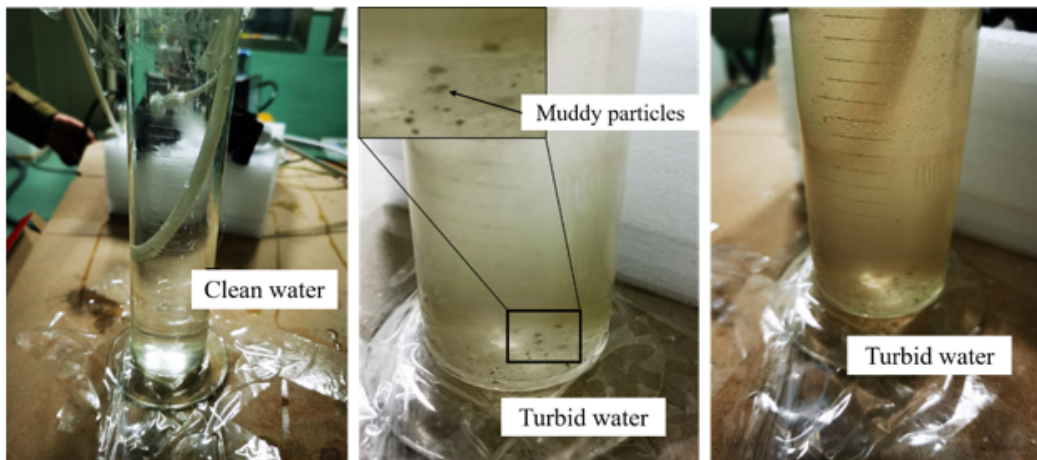


Figure 8

Water turbidity comparison during the loading process

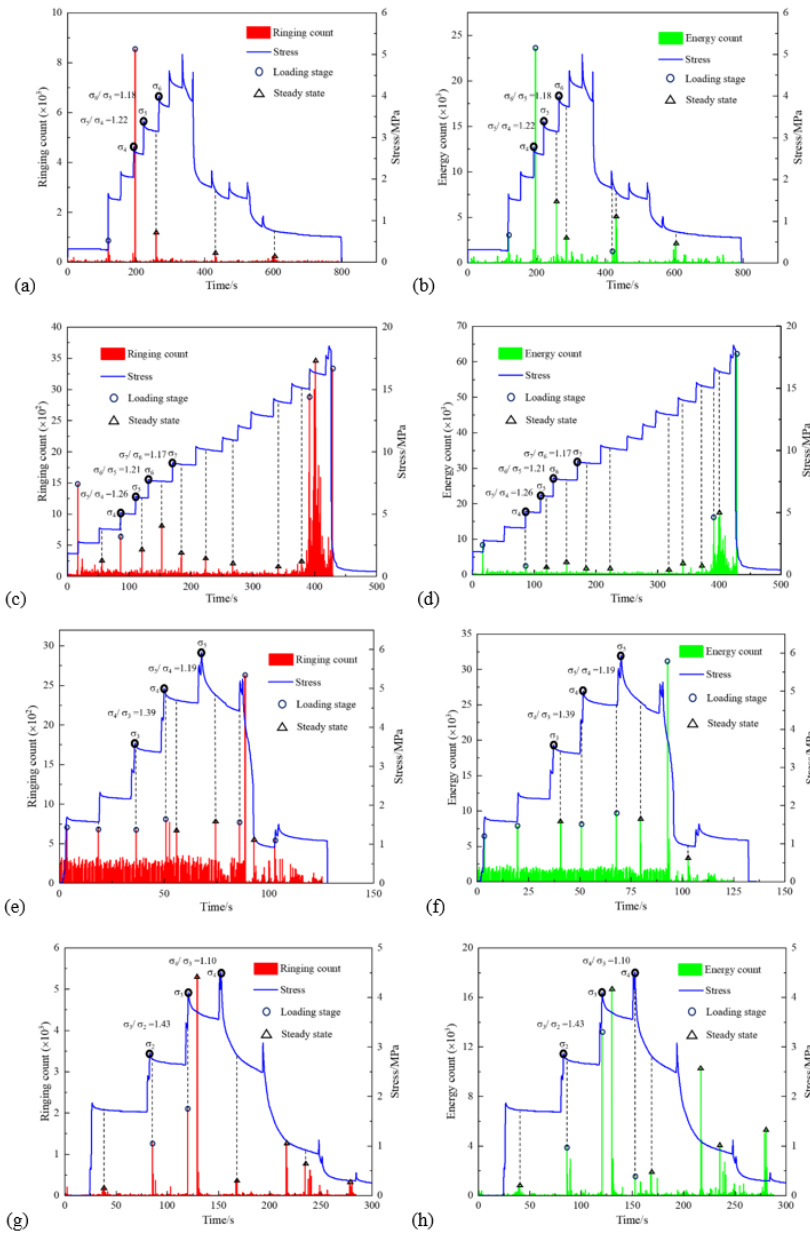


Figure 9

The relationship between stress and the acoustic emission (AE) signal during rock fracture. (a), (c), (e), and (g) correspond to the relationship between stress and ringing count for RBSR01, RBSR02, RBSR03, and RBSR04, respectively; (b), (d), (f), and (h) correspond to the relationship between stress and energy count of RBSR01, RBSR02, RBSR03, and RBSR04, respectively

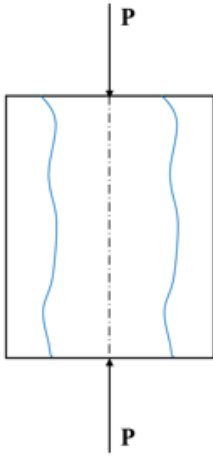


Figure 10

Diagram showing the main failure mode of red-bed mudstone under uniaxial compression

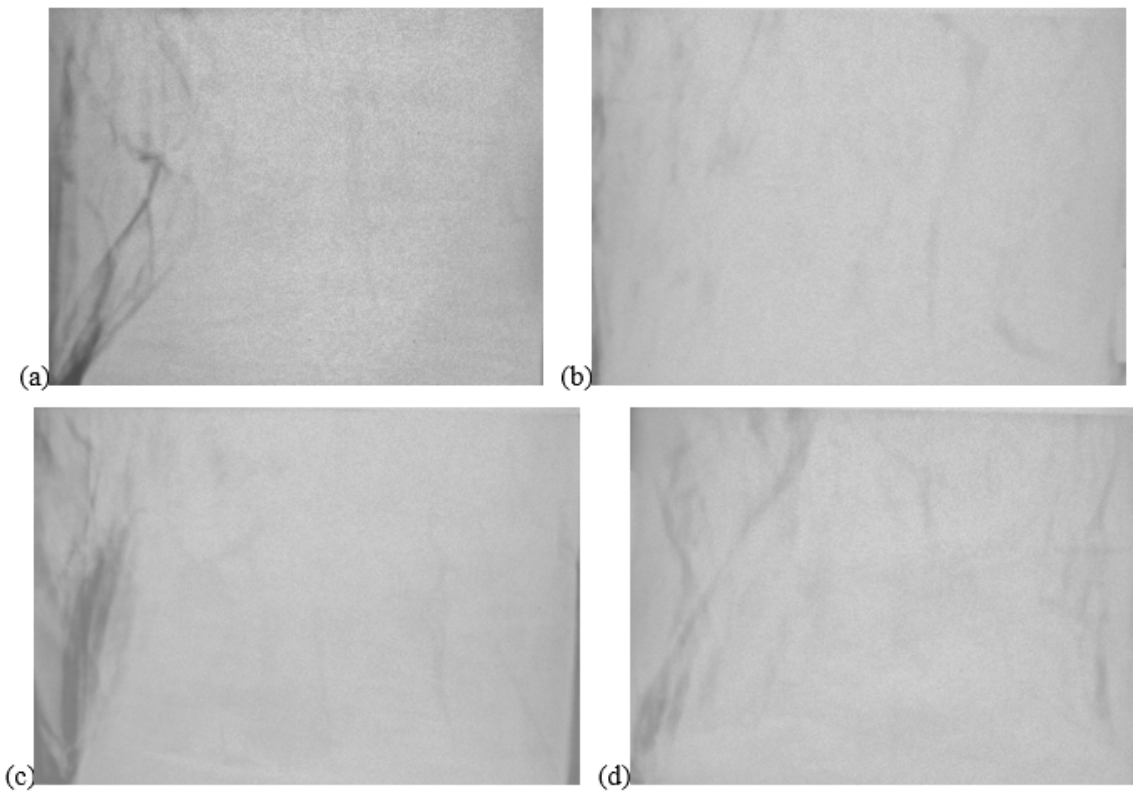


Figure 11

The ultimate failure mode of (a) RBSR01, (b) RBSR02, (c) RBSR03, and (d) RBSR04

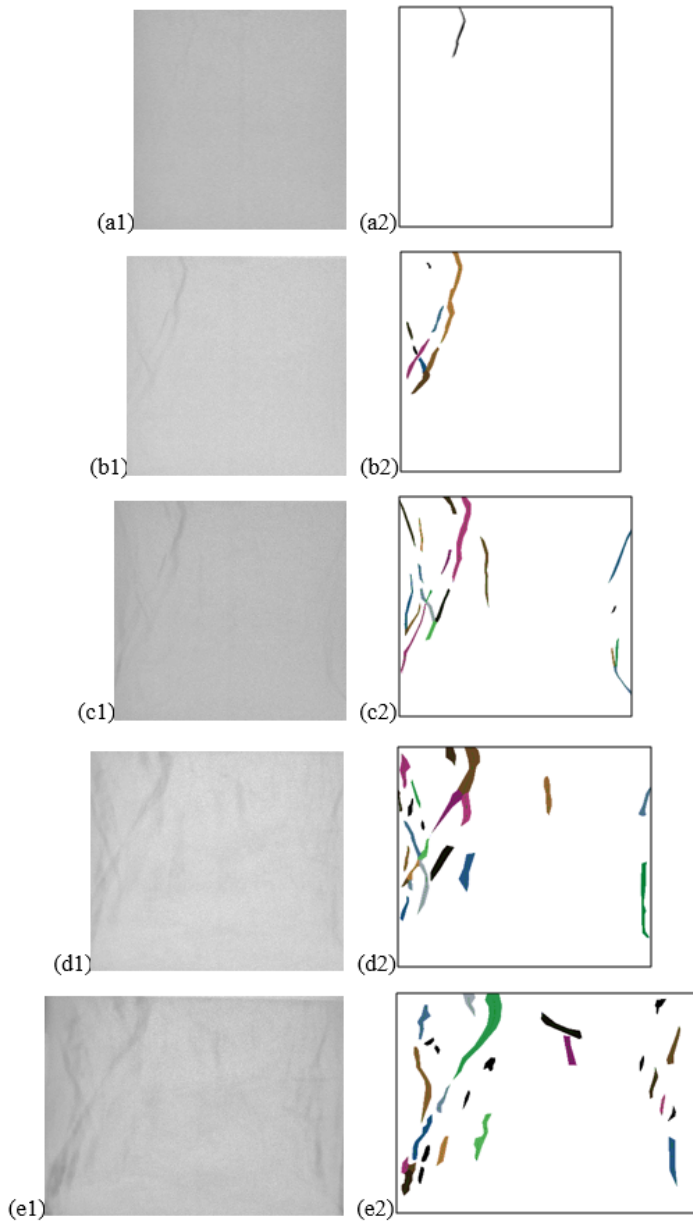


Figure 12

Crack evolution during the failure process of RBSR04. (a1–e1) show DR images and (a2–e2) show extracted crack images

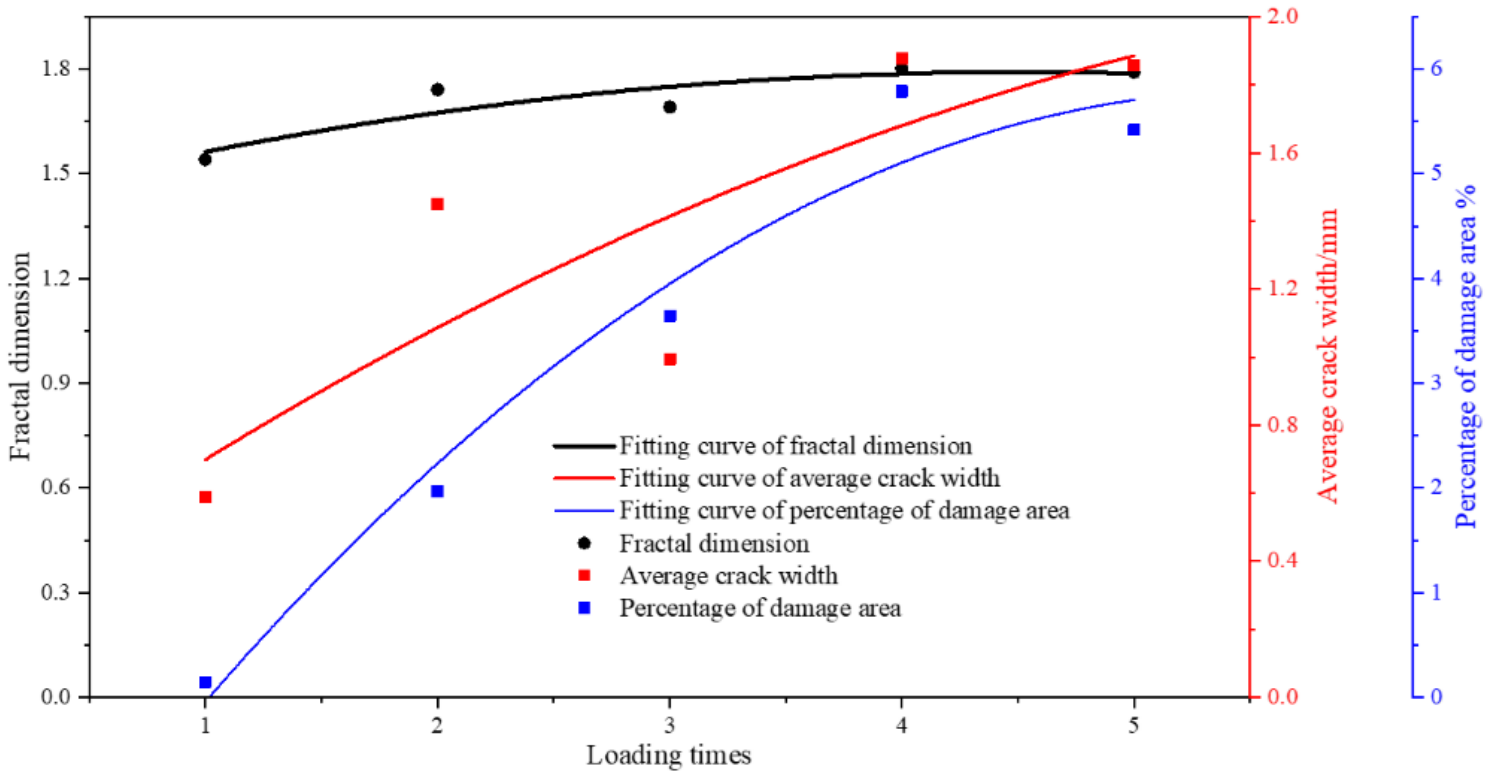


Figure 13

The evolution of fractal dimension, average crack width, and damage area during the failure process for RBSR04. Note: the loading times in the figure start from the loading level at which cracks were first observed in the DR images

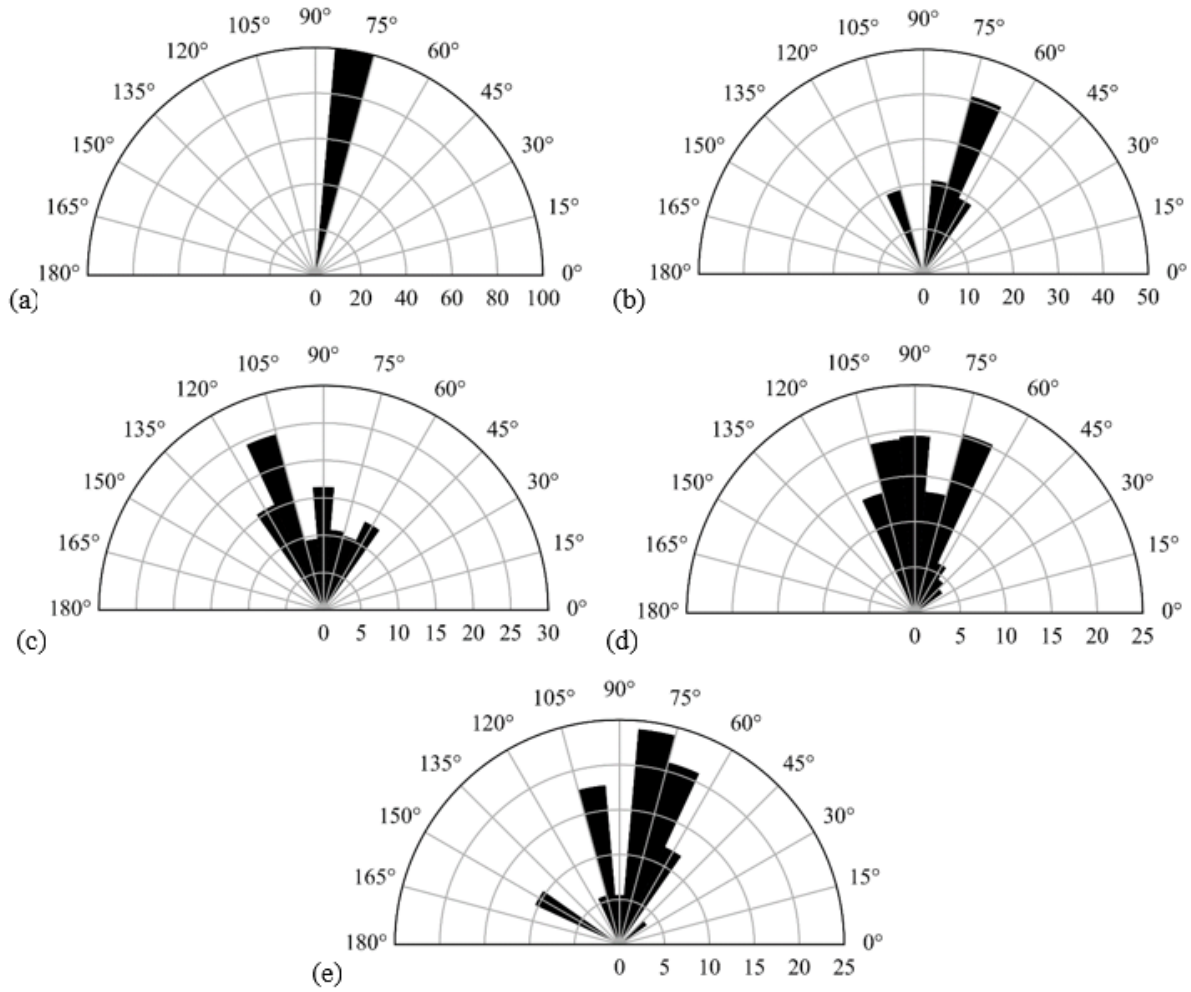


Figure 14

Rose diagram showing the relative distribution of the crack orientation for RBSR04